Evaluation of Precipitation Estimates by at-Launch Codes of GPM/DPR Algorithms Using Synthetic Data from TRMM/PR Observations

Takuji Kubota, *Member, IEEE,* Naofumi Yoshida, Shinji Urita, Toshio Iguchi, *Member, IEEE,*
Shinta Seto, *Member, IEEE,* Robert Meneghini, *Senior Member, IEEE,*
Jun Awaka, *Member, IEEE,* Hiroshi Hanado, *Member, IEEE,*
Satoshi Kida, and Riko Oki

Abstract—The Global Precipitation Measurement (GPM) Core Observatory will carry a Dual-frequency Precipitation Radar (DPR) consisting of a Ku-band precipitation radar (KuPR) and a Ka-band precipitation radar (KaPR). In this study, "at-launch" codes of DPR precipitation algorithms, which will be used in GPM ground systems at launch, were evaluated using synthetic data based upon the Tropical Rainfall Measuring Mission (TRMM) Precipitation Radar (PR) data. Results from the codes (Version 4.20131010) of the KuPR-only, KaPR-only, and DPR algorithms were compared with "true values" calculated based upon drop size distributions assumed in the synthetic data and standard results from the TRMM algorithms at an altitude of 2 km over the ocean. The results indicate that the total precipitation amounts during April 2011 from the KuPR and DPR algorithms are similar to the true values, whereas the estimates from the KaPR data are underestimated. Moreover, the DPR estimates yielded smaller precipitation rates for rates less than about 10 mm/h and greater precipitation rates above 10 mm/h. Underestimation of the KaPR estimates was analyzed in terms of measured radar reflectivity (Z_m) of the KaPR at an altitude of 2 km. The underestimation of the KaPR data was most pronounced during strong precipitation events of $Z_m < 18$ dBZ (high attenuation cases) over heavy precipitation areas in the Tropics, whereas the underestimation was less pronounced when the $Z_m > 26$ dBZ (moderate attenuation cases). The results suggest that the underestimation is caused by a problem in the attenuation correction method, which was verified by the improved codes.

Index Terms—Algorithms, attenuation, Global Precipitation Measurement (GPM), rain, simulation, snow, spaceborne radar, Tropical Rainfall Measuring Mission (TRMM).

I. INTRODUCTION

THE Global Precipitation Measurement (GPM) Mission consists of a Tropical Rainfall Measuring Mission (TRMM)-like nonsun-synchronous orbiting satellite (GPM Core Observatory) and a constellation of satellites carrying microwave radiometer instruments [1]. The GPM Core Observatory, which will be launched in early 2014, carries the Dual-frequency Precipitation Radar (DPR) developed by the Japan Aerospace Exploration Agency (JAXA) and the National Institute of Information and Communications Technology (NICT) [2], and the GPM microwave imager (GMI) provided by the U.S. National Aeronautics and Space Administration (NASA). The DPR consists of two radars: Ku-band (13.6 GHz) PR (KuPR) and Ka-band (35.55 GHz) radar (KaPR). To obtain a higher sensitivity, the DPR employs the variable pulse repetition frequency (VPRF) technique [3], [4]. The DPR is expected to advance precipitation science by expanding the coverage of observations to higher latitudes than those obtained by the TRMM Precipitation Radar (PR), by measuring snow and light rain via high-sensitivity observations from the KaPR, and by providing drop size distribution (DSD) information based on the differential scattering properties of the two frequencies. The combined use of PR and the TRMM microwave imager (TMI) onboard the TRMM satellite has greatly improved the technique of rainfall estimation [5]–[12]. By simultaneous observation with the DPR, the GMI will improve the accuracy of rainfall/snowfall estimates, and work as a bridge between the highly accurate observation by the GPM Core Observatory and frequent observations by constellation satellites with microwave radiometers.

For operational productions of precipitation datasets, it is necessary to develop computationally efficient, fast-processing DPR Level-2 (L2) algorithms that can provide estimated precipitation rates, radar reflectivity factors, and precipitation information, such as the DSD and precipitation type. The L2 algorithms have been developed by the DPR Algorithm Development Team under the NASA-JAXA Joint Algorithm Team [13], [14].

As a test bed for the DPR L2 algorithms, synthetic DPR Level-1 (L1) data are needed before the launch of the GPM Core Observatory. Previous work on algorithm development relied on airborne dual-frequency radar data [15]–[20], ground-based radars [21]–[23], numerical model simulations [24]–[26], and data simulated from the TRMM/PR [27]–[31]. In this paper, we

use the last of these approaches. The primary advantage is that measured Ku-band data from the TRMM/PR, obtained under a wide variety of meteorological conditions, forms the basis of the simulation. As such, the results can be compared directly to the standard TRMM/PR retrievals. The disadvantage is that the hydrometeor particle size distribution and phase state are derived from the PR algorithm results to convert the Ku-band measured reflectivity factors to those at Ka-band.

This paper presents evaluations of "at-launch" codes of the DPR algorithms using the synthetic data generated from the TRMM/PR observations. Section II describes the data and methods related to the GPM/DPR algorithms and synthetic radar data from the PR data. Section III presents an evaluation of the at-launch codes. Section IV provides the horizontal distribution of frequencies in the simulated radar reflectivity of the KaPR. Section V discusses reasons for the underestimates in the KaPR data found in the current code. Section VI presents an overall summary of this research.

II. DATA AND METHODS

A. Antenna Scanning Geometry of the DPR

The antenna scanning geometry of the DPR is needed to generate the synthetic data. Fig. 1 shows the antenna scanning geometry of the KuPR and the KaPR [2]. The KuPR beam scanning from the 13th to the 37th angle-bins and the KaPR beam scanning from the 1st to the 25th angle-bins are performed synchronously to provide matched KuPR and KaPR beams within an accuracy of 1 km. The range resolution is 250 m, and the sensitivity is 0.5 mm/h for both the KuPR and the KaPR in this matched beam portion of the swath. Here, the pixels of the KaPR are referred to as "KaMS," where "MS" denotes the matched portion of the swath. During the time when the KuPR scans the outer swath area (from the 1st to the 12th and from the 38th to the 49th angle-bins) with a range resolution of 250 m, the KaPR scans the interlaced scan area (from the 26th to the 49th angle-bins) with a range resolution of 500 m. The KaPR minimum detectable precipitation rate is 0.2 mm/h in the interlaced scan area. The high-sensitivity pixels of the KaPR are referred as to "KaHS" in this paper. For all the modes and for both frequencies, the beam width is about 0.7°, and the horizontal resolution on the ground is about 5.2 km for both the KuPR and the KaPR when the orbit altitude is 407 km. The KuPR swath width is approximately 245 km, which corresponds to ±17° electrical beam scanning. The KaPR swath width is approximately 125 km, which corresponds to ±8.5° electrical beam scanning. The sampling interval of the KuPR along the range direction is 125 m from the surface up to a height of 14 km, and 250 m for heights from 14 to 19 km. The sampling interval of the KaMS is the same as that of the KuPR, and it is 250 m for all heights in the KaHS.

B. "At-launch" Codes of GPM/DPR Level-2 Algorithms

The "at-launch" codes of the DPR-L2 algorithms will be used in GPM ground systems at the launch for the production of the precipitation datasets. The L2 algorithms will produce three sets of outputs: 1) KuPR-only products, 2) KaPR-only products, and 3) DPR products using both KuPR and KaPR data. It is important
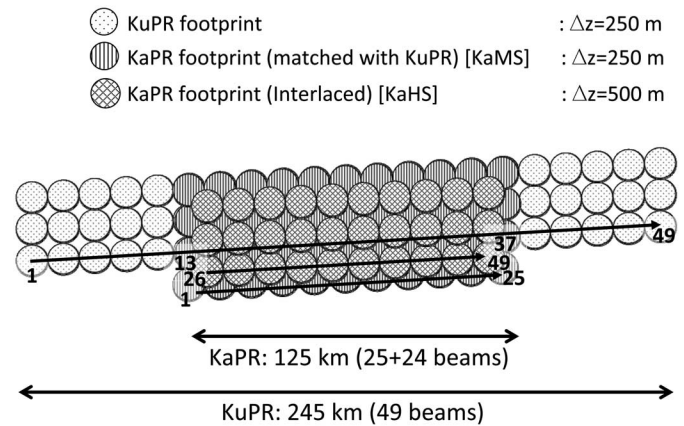
Fig. 1. Schematic of the antenna scanning geometry in the KuPR and KaPR.

to develop algorithms applicable to both PR and KuPR in order to produce a long-term continuous dataset. Thus, the L2 algorithms consist of KuPR, KaPR, and DPR algorithms. The KuPR-L2 algorithm generates the KuPR-L2 product from the KuPR-L1 product that includes Ku-band radar received power data. The KaPR-L2 algorithm generates the KaPR-L2 product from the KaPR-L1 product that includes Ka-band radar received power data. The KaMS and the KaHS data are processed as a single file in the KaPR L1 or L2 product. The DPR-L2 algorithm generates the DPR-L2 product from the KuPR-L2 and the KaPR-L2 products.

While the single-frequency L2 algorithms have been developed based on TRMM/PR standard algorithms [32]–[36], there are several features in the newly developed DPR-L2 algorithm. In the classification module, which classifies precipitation types and bright band information, the KuPR and KaPR algorithms use a concept similar to the PR 2A23 algorithm [36]. However, the DPR algorithm uses the dual-frequency ratio (DFR) method [37], [38]. In the surface reference technique (SRT) module, which estimates the path-integrated attenuation (PIA) for precipitation pixels, the KuPR and KaPR algorithms employ an approach similar to the PR 2A21 algorithm [33], [34], whereas the DPR algorithm uses a dual-frequency SRT (DSRT) based upon the differential path attenuation between the Ku-band and Ka-band [20], [39]. In the Solver (SLV) module, which numerically solves the radar equations and obtains DSD parameters at each range bin, the KuPR and KaPR algorithms use a combination of the Hitschfeld–Bordan attenuation correction method (HB method) and the SRT method, similar to the PR 2A25 algorithm [32], [35]. The DPR algorithm uses a combination of the HB method, the DFR method, and the SRT method [31], [40].

C. KaPR Sampling Experiments by TRMM/PR

Since November 1997, the first spaceborne PR (PR) has been operating on the TRMM satellite. The TRMM/PR operates at a frequency of 13.8 GHz [41], [42], whereas the KuPR of the DPR will operate at 13.6 GHz. The peak transmit power of the TRMM/PR is 500 W, while that of the KuPR is 1012 W.

The antenna scanning geometry of the TRMM/PR and the KuPR, as described in Section II-A, are identical. On the other hand, the scanning geometry of the KaPR is different from that of TRMM/PR. An experiment, in which the scanning geometry of
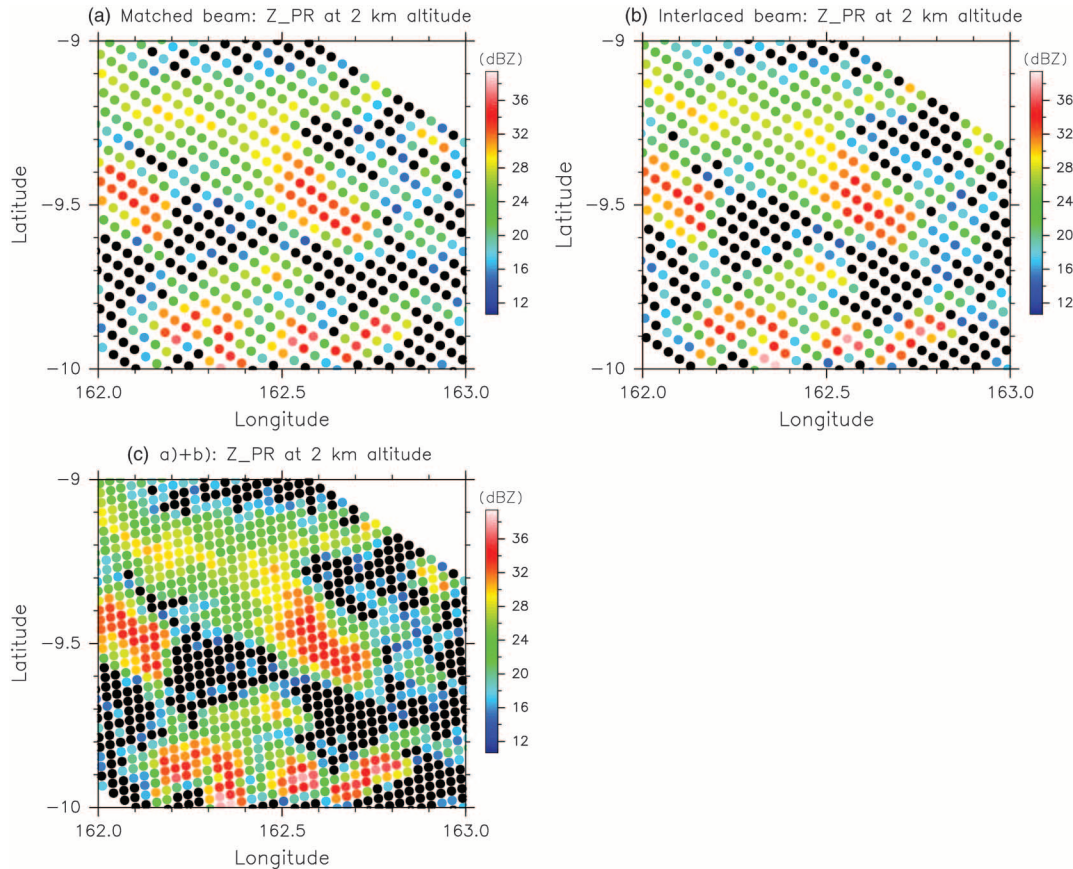
Fig. 2. Examples of measured radar reflectivity data (Z_m) of the TRMM/PR over the southwestern Pacific in (a) matched beams, (b) interlaced beams, and (c) all beams in the TRMM orbit number 53° 160 during the KaPR sampling experiment. Black circles denote pixels where the received power was below the noise level.

the TRMM/PR was modified to that of the KaPR, was desirable in order to produce synthetic data simulating the KaPR scanning geometry. Therefore, JAXA carried out the experiment of the TRMM/PR on March 15, 2007 [43]. The scan angles and the measurement sequence of the PR were modified by sending operational control commands from the ground system. This was referred to as the "KaPR sampling experiment." There were two kinds of operational modifications for the simulation of the KaPR sampling in the experiment. One was a change in the scanning angles and another was a change in the recording range bins. Scanning angles from 1st to 12th and from 38th to 49th were changed by replacing phase codes from the ground system for collecting interlaced footprint data. By this procedure, the TRMM/PR scan range was narrowed from ± 17 to $\pm 8.5°$. The experiment was executed for 7 orbits (orbit numbers from 53159 to 53165). For this experiment, the TRMM/PR L1 algorithm was modified to account for changes in the scan angles and altitude limits. Fig. 2 shows examples of measured radar reflectivity factor (Z_m) data of the TRMM/PR over the southwestern Pacific for TRMM orbit number 53 160 during the KaPR sampling experiment. The matched beams in Fig. 2(a) were identical to half of the normal number of observation beams, and the interlaced beams in Fig. 2(b) correspond to unique observations in this experiment. As a result, observations of scanning geometry similar to the KaPR were obtained as shown in Fig. 2(c).

Moreover, the PR L2 version 6 (V6) algorithms were applied to the experimental data for computing precipitation rates. Note

that this experiment was executed in the scanning simulation and the radar frequency was fixed at 13.8 GHz. Therefore, Z_m values of the DPR were estimated by the method described in Section II-D. Nevertheless, the experimental data are valuable for evaluation of the L2 algorithms because observations of the interlaced scan are unique. In this study, evaluations of the KaHS were performed using only the KaPR sampling experimental data.

D. Development of Synthetic Radar Data

This section describes how the synthetic DPR L1 data are generated from the PR data. Here, the DSD, N(D) was modeled by a gamma distribution function of a drop diameter D, as shown in the following equation:

$$N(D) = N_0 D^\mu \exp[-(3.67 + \mu)D/D_0]$$

Two DSD parameters (N_0, D_0) were retrieved from the effective radar reflectivity factor (Z_e) and specific attenuation (k) obtained in the PR 2A25 product based upon the method of Seto *et al.* [31]. Third parameter of the DSD function μ was assumed to be 3 in this study, because PR 2A25 and current DPR-L2 algorithms adopt this assumption. For each range bin, k/Z_e can be converted to D_0 using the theoretical relationship between k/Z_e and D_0; N_0 is then obtained from D_0 and Z_e. The current relationship was identical to that used in the algorithms. When
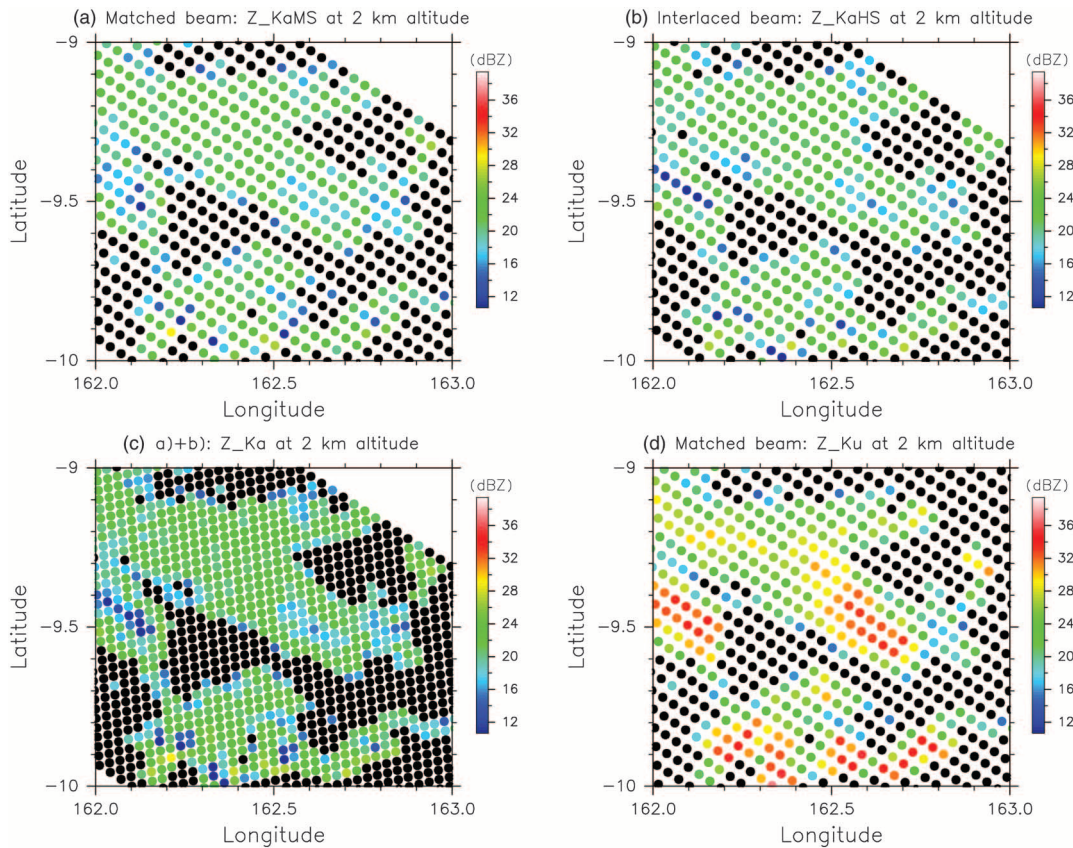
Fig. 3. Same as Fig. 2, except for Z_m of the GPM/DPR synthetic data for (a) matched beams, (b) interlaced beams, (c) all beams at the Ka-frequency, and (d) matched beams at the Ku-frequency.

k/Z_e is not a monotonic function of D_0, the smaller D_0 is selected. Estimates of nonprecipitating constituents of the atmosphere such as water vapor (WV), molecular oxygen (O_2), and cloud liquid water (CLW) were based upon atmospheric information obtained from a Global Objective Analysis from the Japan Meteorological Agency (GANAL). Attenuation due to WV was estimated by a formulation presented in previous work [44]–[46], and attenuation due to O_2 was estimated by a formulation presented in similar and other previous work [45]–[47]. Attenuation due to CLW was estimated for nonprecipitating pixels from GANAL and for precipitating pixels from a CLW database generated by global cloud-resolving model simulations as a function of surface precipitation rate, temperature, and precipitation type [48]. Thus, PIA and Z_m of KuPR and KaPR were calculated from the estimated DSD with attenuations.

In the surface echo simulation at the Ka-band, it is necessary to consider differences of the normalized radar cross section (NRCS) between the Ku-band and the Ka-band frequencies. In this study, statistical mean differences of the NRCS, which are dependent upon incidence angles, were used from dual-frequency airborne radar results [19], [20]. This simple assumption is reasonable over the ocean background because quasi-specular scattering dominates when the incident angle is less than $20°$. On the other hand, the NRCS of over the land background is often modeled by the soil surface and vegetation cover [49]–[52] and this assumption may be problematic here. The relationships between the KuPR and the KaPR for Z_e and the NRCS, described

in Appendix A, were used in the calculation. For the values of Z_e at the surface, the difference in Z_e between the KuPR and the KaPR is directly related to the difference between the NRCS at the two frequencies. Furthermore, the surface echo at the Ka-band was calculated considering differences of PIA by the precipitation and nonprecipitation between the Ku-band and Ka-band frequencies. In the simulation, the surface echo at KuPR was assumed to be the same as that of the TRMM/PR.

Using these atmospheric and surface models, the radar return power can be calculated from Z_m at KuPR/KaPR according to the appropriate radar equation. In this study, constant noise levels were taken to be -109.50 dBm at KuPR, -109.47 dBm at KaMS, and -112.48 dBm at KaHS. Finally, the received power data were resampled using the VPRF table and archived in the KuPR/KaPR L1 format. Fig. 3 shows comparisons of Z_m in the DPR synthetic data at a 2 km altitude over the southwestern Pacific. Due to higher attenuation at Ka-band by precipitation and other atmospheric constituents, Z_m values at Ka-band were lower in stronger precipitation areas than Z_m values at Ku-band. Note that the synthetic data were computed at pixels where the PR algorithm identified "rain" (i.e., data were recorded with a "rain certain" flag). Therefore, radar reflectivity data diagnosed as "no-rain" or "rain possible" by the PR L1 algorithm were not calculated in the current simulation. This was done because the simulation is based on Z_e data in the 2A25 product. Thus, weak signals diagnosed as "no-rain" or "rain possible" in the PR were omitted in KuPR/KaPR Z_m, as shown in Fig. 3. This constitutes a limitation of the current synthetic dataset.
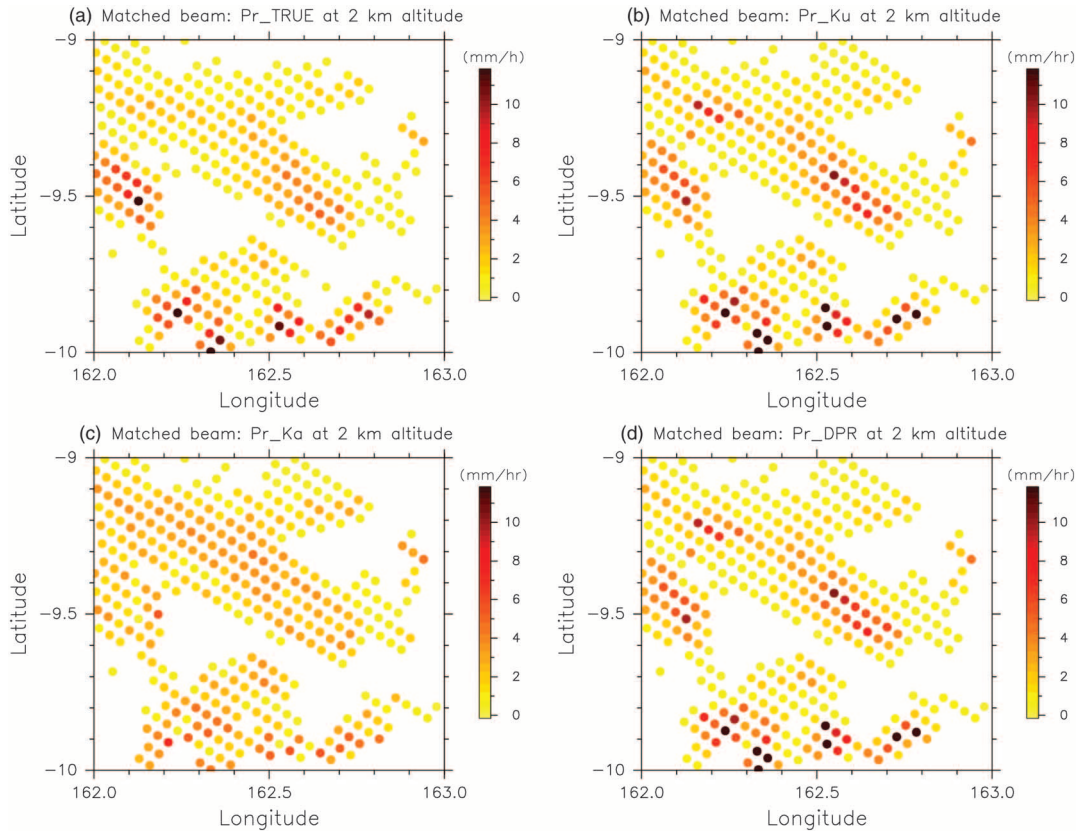
Fig. 4. Same as Figs. 2 and 3, except for precipitation rates at an altitude of 2 km in matched beams of (a) true values, (b) KuPR, (c) KaMS, and (d) DPR.

Following the methodology described above, synthetic DPR L1 data were produced for 1 month from April 1 to 30, 2011 based upon the PR version 7 (V7) products. These datasets, along with the data from the KaPR sampling experiment data on March 15, 2007 described in Section II-C, were used as test data for the DPR level-2 algorithms.

III. EVALUATION OF GPM/DPR LEVEL-2 "AT-LAUNCH" ALGORITHMS

This section provides evaluations of the at-launch codes of KuPR, KaPR, and DPR L2 algorithms (version 4.20131010) which were submitted in early October 2013. The precipitation rate calculated from the DSD assumed in the synthetic data and a drop size/fall-speed relationship [53] is regarded as the true value in this study. The PR V7 algorithm takes into account nonuniform beamfilling (NUBF) effects [22], [35], [54], whereas the PR V6, KuPR, KaPR, and DPR L2 algorithms do not. Therefore, the NUBF effects were not considered in the calculation of the true values. Thus, the current KuPR, KaPR, and DPR L2 products are compared with the true value data. The radar rain echoes from near the surface are hidden by the surface clutter echo, and precipitation estimates at the lowest point in the clutter-free region (clutter-free bottom) are taken to be near-surface precipitation rates ("nearSurfRain" in the PR 2A25 and "precipRate-NearSurface" in DPR L2 algorithms). However, a routine to detect the surface clutter and the clutter-free bottom, which is one of the new features of the algorithms for the KaPR, is still in the developmental stage. In addition, the clutter-free bottoms can be

different between the KuPR and KaPR. While precipitation rates at the actual surface are estimated by the algorithms assuming a slope in the clutter region ("e_surfRain" in the PR 2A25 and "precipRateEsurface" in DPR L2 algorithms), the results depend upon the location of the clutter-free bottom and the different assumptions used in the PR and DPR algorithms. Thus, a precipitation rate at an altitude of 2 km was adopted as an index of the surface precipitation rate for purposes of the comparisons made for the KuPR, KaPR, and DPR products in this study.

Analyzed precipitation rates at the KuPR and DPR were confined within the KaPR observation swath width, i.e., the 13th to the 37th angle-bins (see Section II-A), for a comparison of the algorithms. Precipitation rates over the interlaced scan area were analyzed in the KaPR product, while those in the DPR product were not. This study focused on over-ocean estimates because the surface echo simulation at Ka-band may be problematic over the land, as was noted in the previous section. Another reason we focused on the ocean is that the surface clutter detection routine is also problematic over the land because of difficulties introduced by complex terrains. This will be one of the future tasks in upgrading the algorithms.

Fig. 4 shows the comparisons made for the precipitation rates at an altitude of 2 km over the southwestern Pacific for TRMM orbit number 53 160 during the KaPR sampling experiment. This specific case study showed that KuPR/DPR-estimates were similar to the true values, while the KaPR estimates were clearly smaller in strong precipitation areas. A comparison between Figs. 3 and 4 suggests that the KaPR estimates obtained by the current algorithm underestimated in stronger precipitation areas.
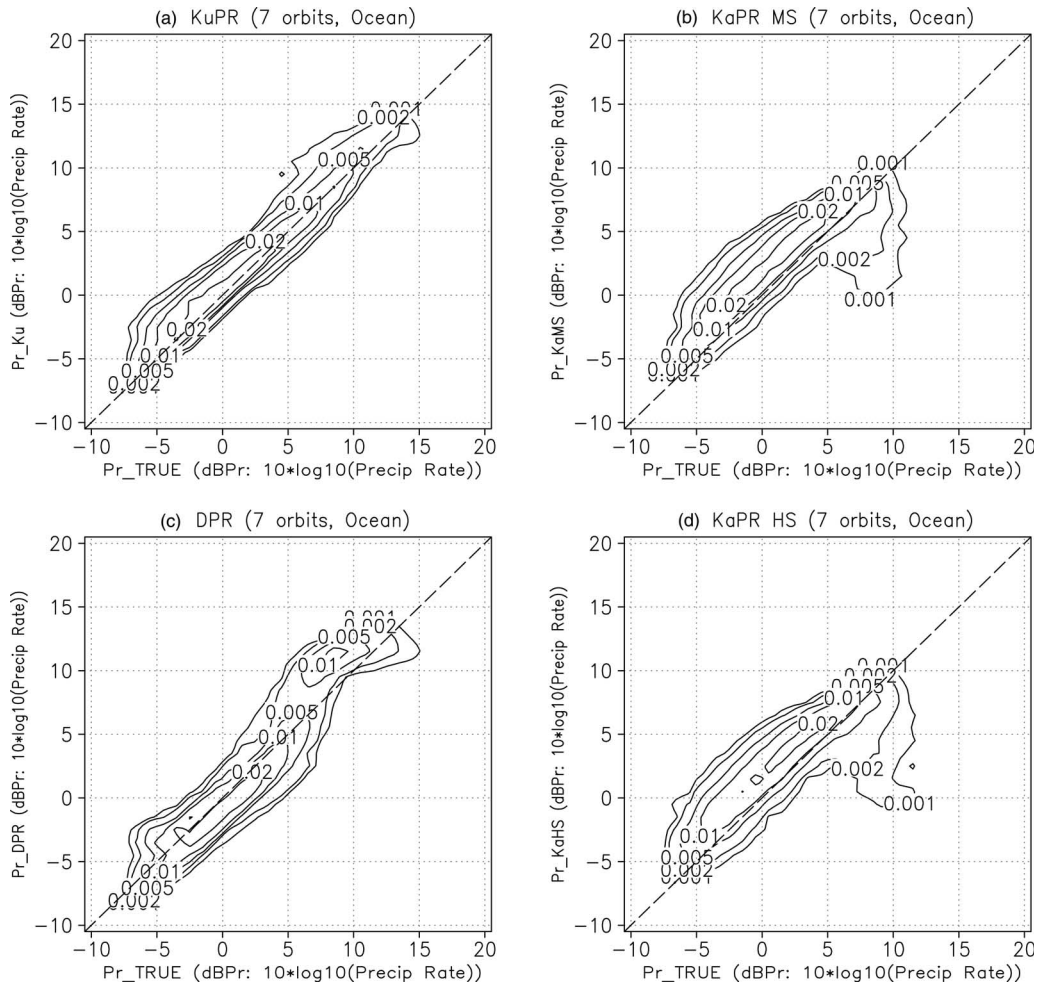
Fig. 5. Pdfs of precipitation rates at an altitude of 2 km over the ocean in 7 orbits during the KaPR sampling experiment. Vertical axes are precipitation rates of (a) KuPR, (b) KaMS, (c) DPR, and (d) KaHS. All horizontal axes are precipitation rates from the true values. A unit of both axes is a decibel of the precipitation rate dBPr, i.e., $10 \times \log_{10}$ (precipitation rate). The values -10, 0, 10, and 20 dB Pr correspond to 0.1, 1.0, 10.0, and 100 mm/h, respectively. Contours show labeled values.

TABLE I
CORRELATION COEFFICIENTS OF KUPR, KAMS, KAHS, AND DPR ESTIMATES WITH THE TRUE VALUES, AND RMSE OF
KUPR, KAMS, KAHS, AND DPR WITH REFERENCE TO THE TRUE VALUES

Statistics	KuPR	KaMS	KaHS	DPR
Correlation coefficients	0.92	0.51	0.47	0.84
RMSE (mm/h)	0.34	0.72	0.84	0.52

A targeting variable is a precipitation rates at an altitude of 2 km. Statistics were analyzed for over-ocean events during the KAPR sampling experiment

Fig. 5 shows probability density functions (pdfs) for precipitation rates at an altitude of 2 km over the ocean for the 7 orbits of the KaPR sampling-experiment data. The units of both axes are taken to be the precipitation rate in decibels dBPr, i.e., $10 \times \log_{10}$ (precipitation rate). The results for the correlation coefficients and the root mean square errors (RMSEs) are summarized in Table I. The KuPR estimates were in good agreement with the true values. For the KaPR results, distinct underestimates were found for precipitation rates of more than 6 dBPr (about 4 mm/h), while overestimates were found for precipitation rates of less than about 4 mm/h. Differences between the KaMS and the

KaHS results were small. This is the result of the fact that no weak signals occur in the synthetic data, as noted in Section II-D. In Fig. 5(c), estimates of the DPR show underestimation in the precipitation rate for values less than 10 mm/h, and overestimation for precipitation rates of above 10 mm/h. The performances of the DPR shown in Table I were slightly worse than those of the KuPR. The DSD in the synthetic data were estimated from the PR 2A25 product, and the relationship between k/Z_e and D_0 in the synthetic data was identical to that used in the algorithms, as described in Section II-D. Thus, the assumptions used in the KuPR-only algorithm are consistent with the assumed DSD
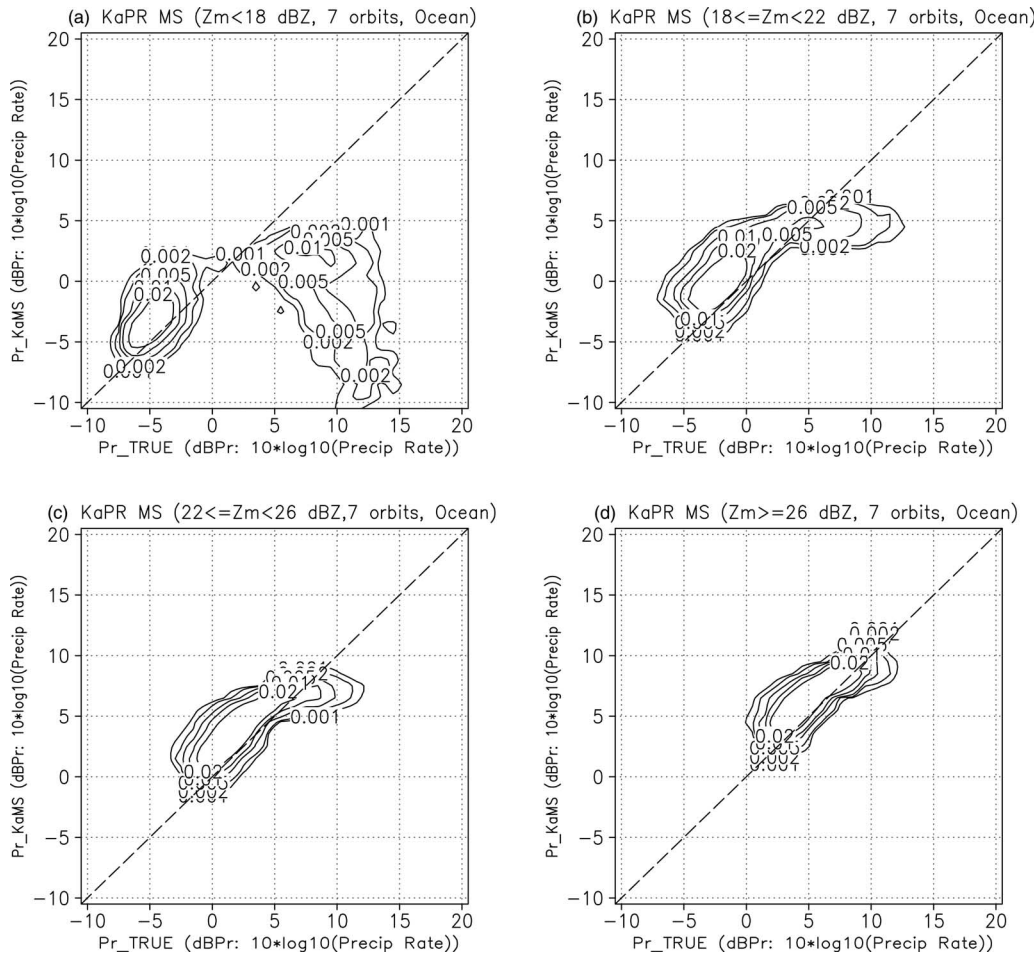
Fig. 6. Same as Fig. 5, except for the KaMS when the Z_m of the KaPR was (a) less than 18 dBZ, (b) between 18 and 22 dBZ, (c) between 22 and 26 dBZ, and (d) more than 26 dBZ.

TABLE II
CORRELATION COEFFICIENTS BETWEEN THE KaMS (VERSION 4.20131010 CODE) AND THE TRUE VALUES WITH
THRESHOLDS OF INTENSITIES FOR THE Z_{mKa}

Statistics	Threshold (Unit: dBZ)			
	$18 < Z_{mKa}$	$18 \le Z_{mKa} < 22$	$22 \le Z_{mKa} < 26$	$Z_{mKa} \le 26$
Correlation coefficients	0.12	0.65	0.72	0.83
Sample number	9619	10322	10605	3345

A targeting variable is a precipitation rates at an altitude of 2 km. Sample numbers are also listed in the table. Statistics were analyzed for over-ocean events during the KaPR sampling experiment.

which provides an accuracy to the KuPR-only algorithm better than what normally can be expected.

The KaPR estimates were further analyzed using the intensity of Z_m of the KaPR (Z_{mKa}) at an altitude of 2 km. Fig. 6 shows pdfs of the KaMS when the values of Z_{mKa} fall into the following categories: less than 18 dBZ, 18–22 dBZ, 22–26 dBZ, and more than 26 dBZ. When the Z_{mKa} is greater than 26 dBZ, the KaPR estimates display good correspondence with the true values [Fig. 6(d)]. Results for the correlation coefficients are summarized in Table II. When the Z_{mKa} is between 18 and 22 dBZ or between 22 and 26 dBZ, the pdfs show a dependence on the magnitude of

the true value [Figs. 6(b) and (c)]. When the true value decreases, the attenuation due to the precipitation also decreases and the KaPR estimates correspond well with the true values. However, underestimation of the KaPR is clearly evident for higher intensities of the true value, corresponding to heavier attenuation along the path. When the Z_{mKa} is less than 18 dBZ, two clusters are found in the pdf [Fig. 6(a)]. One of these corresponds to weak precipitation events of less than 1 mm/h. The other corresponds to stronger precipitation events greater than 4 mm/h that are associated with heavy attenuation. The underestimation of the KaPR most clearly appears during heavy precipitation events where
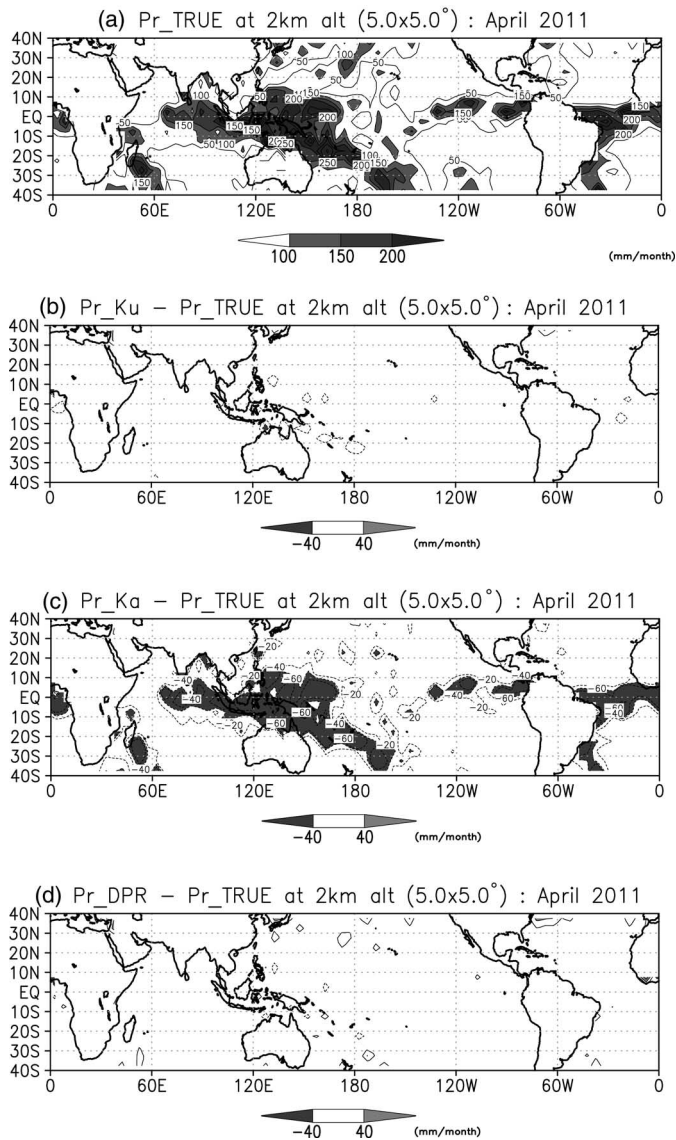
Fig. 7. (a) Precipitation rates at an altitude of 2 km averaged during April 2011 by the true values and differences of (b) KuPR, (c) KaMS, and (d) DPR averaged during April 2011 with reference to the true values.

Fig. 8. Zonally averaged precipitation rates at an altitude of 2 km over the ocean during April 2011. Red, green, blue, black, orange, and light blue lines indicate precipitation rates of KuPR, KaMS, DPR, true values, PR V6, and PR V7, respectively.
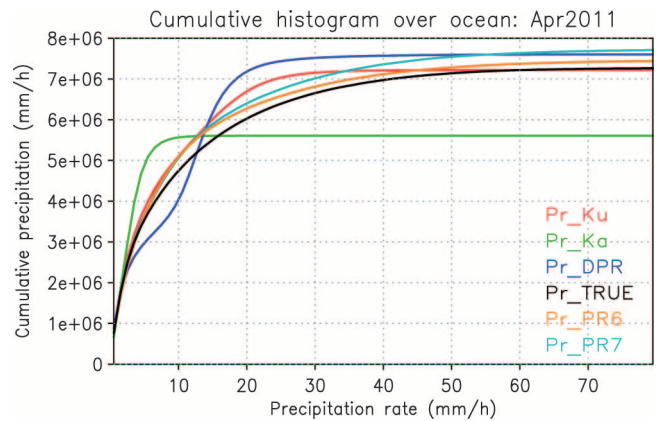
Fig. 9. Cumulative histogram of precipitation rates at an altitude of 2 km over the ocean during April 2011. Lines indicate same data as in Fig. 8. Histogram bins were determined only by precipitation rates. The width of the bin is 1 mm/h.

$Z_{mKa} < 18$ dBZ. The Z_{mKa} value is not always directly connected to a precipitation rate. The Z_e was calculated from the Z_{mKa} by the attenuation correction method and a precipitation rate was calculated from the Z_e considering the DSD. However, the results suggest that underestimation is caused by a problem in the attenuation correction method, because the underestimation was obvious when the $Z_{mKa} < 18$ dBZ (heavy attenuation cases) but less pronounced when the $Z_{mKa} > 26$ dBZ (moderate attenuation cases). Thus, the classification by the Z_{mKa} is related to that of the PIA to some extent. In addition, the classification by the Z_{mKa} can be connected to characteristics of the precipitation, a topic which will be discussed further in Section IV.

Global monthly results are shown in Fig. 7 where the difference in the surface precipitation among KuPR, KaPR, and DPR and the true values are shown. Large underestimations were found in the KaPR, whereas the differences were small in the KuPR and DPR. The underestimations of the KaPR were clear in tropical areas with precipitation amounts heavier than 100 mm/month, whereas the discrepancies were less clear in the mid-latitude areas of the Northern Hemisphere. This is directly related to the frequency of strong precipitation, which is higher in the Tropics than in the mid-latitudes. This feature will be discussed in Section IV. Fig. 8 shows zonally averaged surface precipitation rates over the ocean. Estimates among the PR V6 and V7, KuPR, DPR, and true values were similar in the Tropics, whereas the KaPR algorithm yielded underestimates. In this and following analyses, PR estimates are presented for both the PR V6 and 7 products. Precipitation amounts for the PR V7 estimates, which take the NUBF effects into account, were highest in the Tropics.

Fig. 9 shows the cumulative histogram of precipitation rates during April 2011. As in previous figures, Fig. 9 shows that for the KaPR, there was overestimation at the smaller precipitation rates and underestimation at the larger precipitation rates. On the other hand, the KuPR estimates were larger than the true values for precipitation rates less than 40 mm/h. With reference to the true values, both curves approached similar values for precipitation rates higher than 40 mm/h. These data suggest that the frequencies of stronger precipitation in the KuPR estimates were smaller than those of the true values in the current evaluation. In the histogram, accumulations of the DPR estimates were smaller compared to the

true values and the PR estimates for precipitation rates less than about 13 mm/h and larger for precipitation rates more than about 13 mm/h, while the total precipitation amount was similar between the DPR and PR estimates. This is consistent with the results showing underestimations for precipitation rates less than 10 mm/h and overestimations for precipitation rates above 10 mm/h in Fig. 5(c). Seto *et al.* [31] indicated that estimates of precipitation rates were severely underestimated for rates above 10 mm/h in the HB-DFR method, which does not use the SRT method. The at-launch codes use the HB-DFR-SRT method which is the combination of the DFR, the HB, and the SRT methods. Therefore, larger estimates in precipitation rates above 10 mm/h can be connected to the incorporation of the SRT method. Improvements in the HB-DFR-SRT method for the DPR algorithm will be one of the future tasks conducted for the algorithms.

IV. HORIZONTAL DISTRIBUTION OF FREQUENCIES IN THE SIMULATED Z_m OF THE KAPR

In Section III, distinct underestimations were found in estimates of the KaPR. The analyses show the underestimation was related to the intensity of Z_{mKa} at an altitude of 2 km. In this section, the behavior of the KaPR estimates is discussed from the viewpoint of the horizontal distribution of Z_{mKa}. Fig. 10(a) shows ratios of occurrences in Z_{mKa} larger than 26 dBZ for all precipitation occurrences at a 2 km altitude over the ocean averaged over all data from April 2011. Here, the ratio is referred to as "$RA_{26} \leq Z_{mKa}$", where the subscript denotes the threshold. Through a comparison of precipitation amounts shown in Fig. 7(a), higher $RA_{26} \leq Z_{mKa}$ values indicate a "horseshoe" pattern in the Pacific, which is located in areas neighboring heavy precipitation regions. Lower ratios were found in the subtropical Pacific Ocean where shallow weak precipitation is dominant. In addition, higher ratios were found in the mid-latitudes and in small areas of the Atlantic and Indian Oceans. Fig. 6(d) shows good correspondence with reference to the true precipitation rate over the area with this threshold. Ratios of occurrences in the Z_{mKa} between 18 and 26 dBZ ($RA_{18} \leq Z_{mKa} < 26$) were relatively high throughout the TRMM domain, except for regions in the subtropical waters of the Pacific and Atlantic Oceans, and the Arabian Sea [Fig. 10(b)].

In the analysis of the ratios of Z_{mKa} for values smaller than 18 dBZ, the intensity of the true precipitation rate was used because Fig. 6(a) showed two clusters that depended on the magnitude of the true precipitation rate. A threshold of 4 mm/h in the precipitation rate at an altitude of 2 km was adopted here. Fig. 11(a) shows $RA_{ZmKa < 18\&Pr > 4}$ with precipitation rates stronger than 4 mm/h. This threshold corresponds to a clear underestimation of the KaPR due to stronger precipitation attenuation, as shown in Fig. 6(a). The horizontal pattern of the $RA_{ZmKa < 18\&Pr > 4}$ corresponds to occurrences of heavy attenuation, which are similar to the distribution of large differences of precipitation rates between the KaPR estimates and the true values as in Fig. 7(c). Higher ratios of the $RA_{ZmKa < 18\&Pr > 4}$ were found in the Tropics, but not in the mid-latitude area of the Northern Hemisphere. This can be related to the frequency of strong precipitation, which is higher in the Tropics than in mid-latitudes. Fig. 11(b) shows $RA_{ZmKa < 18\&Pr \leq 4}$ with precipitation
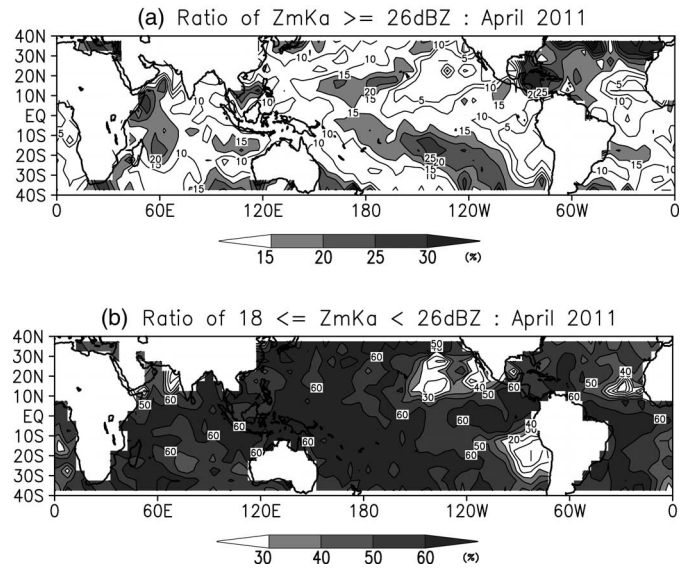
Fig. 10. Ratios of occurrences in Z_m of the KaPR a) larger than 26 dBZ and b) between 18 and 26 dBZ for all precipitation occurrences at an altitude of 2 km over the ocean averaged during April 2011. The unit is a percentage (%).
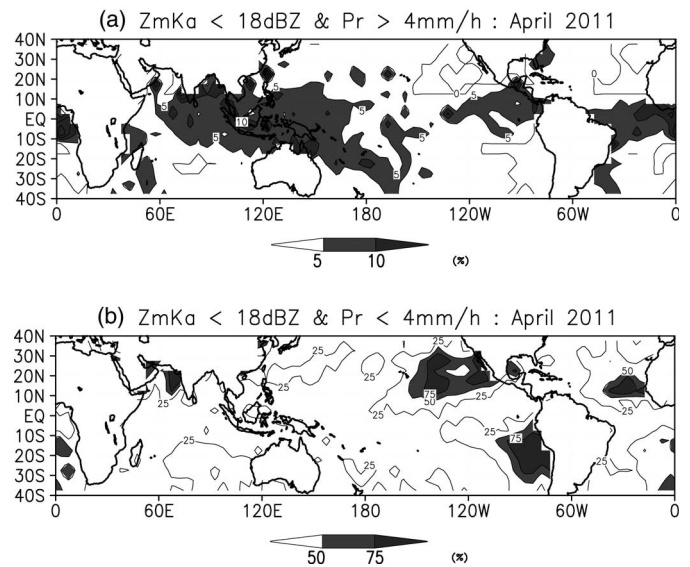
Fig. 11. Ratios of occurrences in Z_m of the KaPR smaller than 18 dBZ for all precipitation occurrences at an altitude of 2 km over the ocean averaged during April 2011. Ratios were classified with precipitation rates of the true values (a) larger than 4 mm/h and (b) smaller than 4 mm/h. The unit is a percentage (%).

rates less than 4 mm/h. In this figure, higher ratios were clearly found in subtropical waters of the Pacific Ocean, the Atlantic Ocean, and the Arabian Sea.

Thus, classification by the Z_{mKa} with the precipitation thresholds demonstrated important characteristics of the precipitation, even though the Z_{mKa} value is not always directly connected to the precipitation rate.

V. DISCUSSION

In the evaluations using the at-launch codes (version 4.20131010) of the KaPR L2 algorithm, distinct underestimations were found for precipitation rates of more than about 4 mm/h, as
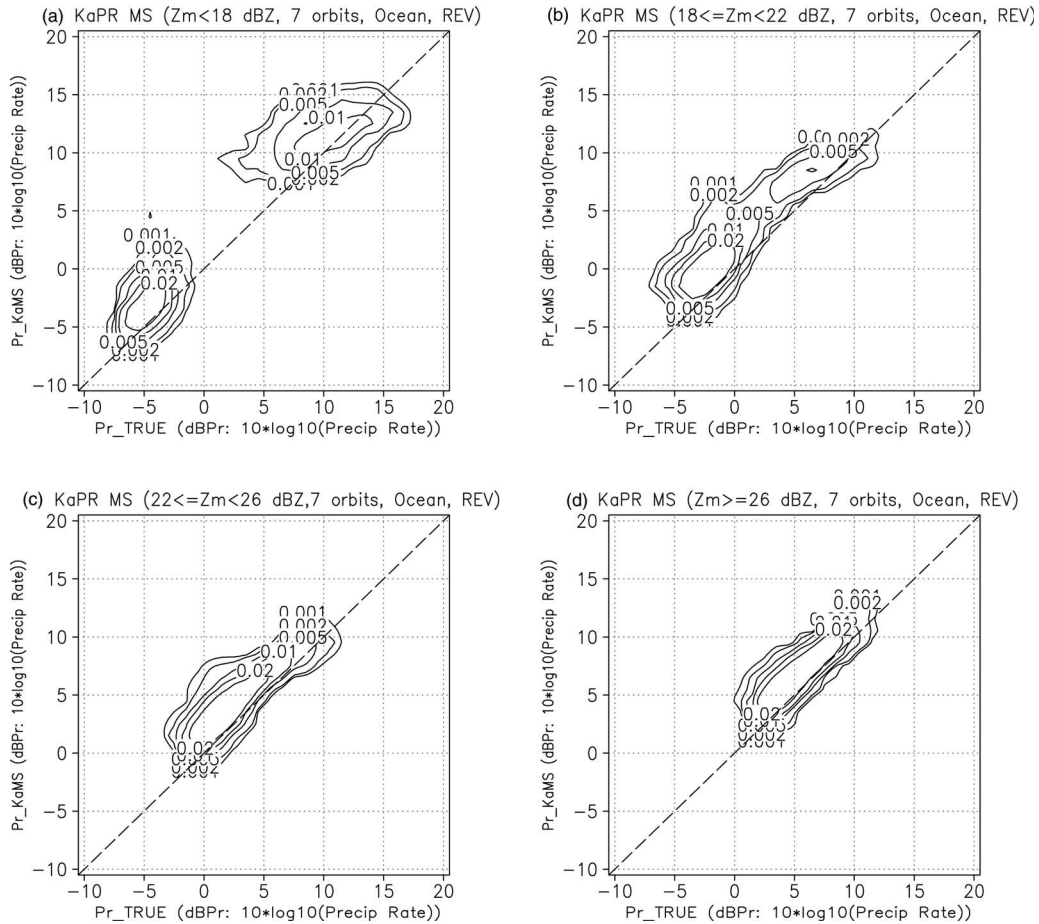
Fig. 12. Same as Fig. 6, except for the KaMS by the version 4.20131129 code.

TABLE III
SAME AS TABLE 2, EXCEPT FOR THE KaMS BY THE VERSION 4.20131129 CODE

Statistics	Threshold (Unit: dBZ)			
	$18 < Z_{mKa}$	$18 \leq Z_{mKa} < 22$	$22 \leq Z_{mKa} < 26$	$Z_{mKa} \leq 26$
Correlation coefficients	0.78	0.86	0.84	0.86
Sample number	9619	10322	10605	3345

described in Section III. The underestimation of the KaPR data was most pronounced during strong precipitation events where $Z_{mKa} < 18$ dBZ (high attenuation cases) which occurred in heavy precipitation areas of the Tropics. Underestimation was less pronounced in the moderate attenuation cases where $Z_{mKa} \geq 26$ dBZ. The results suggested that the underestimation was caused by a problem in the attenuation correction method.

In order to verify this, results from the upgraded code (version 4.20131129) of the KaPR L2 algorithm, which was submitted as the operational at-launch code at the end of November 2013, are analyzed in this section. In the version 4.20131129 code, the SLV module uses an improved version of the attenuation correction method. Fig. 12 shows pdfs of the KaMS from the version 4.20131129 code using 7 orbits of the KaPR sampling experiment data. In contrast with Fig. 6, the KaMS estimates from this version were in good agreement with the true values for moderate values of

the attenuation, whereas the KaMS estimates underestimate for precipitation intensities above about 15 dBPr (about 32 mm/hr) in precipitation events for which $Z_{mKa} < 18$ dBZ [Fig. 12(a)]. Results for the correlation coefficients are summarized in Table III. In the comparisons shown in Tables II and III, the correlation coefficients were higher for version 4.20131129 than for version 4.20131010 in all Z_{mKa} ranges. These results clearly show that the underestimates in version 4.20131010 code were caused by deficiencies in the attenuation correction method of the SLV module and that this problem has been resolved in the latest version of the SLV module.

VI. SUMMARY

In this study, the "at-launch" codes of the GPM/DPR L2 algorithms (version 4.20131010) were evaluated using synthetic data generated from TRMM/PR data. There are three sets of L2

algorithms corresponding to algorithms that process KuPR data only (KuPR), KaPR data only (KaPR), and DPR products using both KuPR and KaPR data. Synthetic DPR L1 data were produced for 1 month from April 1 to 30, 2011. In addition, TRMM/PR experimental data on15 March 2007 was used to simulate the KaPR scanning geometry.

This study focused on evaluating the estimated precipitation rates from the single and dual-frequency algorithms (version 4.20131010) at a 2 km altitude over ocean within the 125 km KaPR observation swath width. A precipitation rate calculated from the assumed DSD in the synthetic data was regarded as the true value in this study. The total precipitation amounts estimated from among the true values, the PR V6 and V7, KuPR, and DPR products during April 2011 were similar in the Tropics, whereas values from the KaPR underestimated precipitation in this region. The DPR estimates were smaller for precipitation rates less than 10 mm/h and larger for precipitation rates above 10 mm/h compared to the true values, whereas the total precipitation amount from the DPR was similar to the true value. Improvement of the combination of the HB, the DFR, and the SRT methods in the DPR algorithm will be one of future tasks.

Precipitation rates of the KaPR showed an underestimation at higher precipitation rates. Underestimation of the KaPR estimates was analyzed by using the intensity of Z_{mKa} at an altitude of 2 km. The quantity of Z_{mKa} is related to the PIA to some extent, and can be connected to characteristics of the precipitation. The underestimation was clear when $Z_{mKa} < 18$ dBZ (heavy attenuation cases) but less obvious when the $Z_{mKa} \geq 26$ dBZ (moderate attenuation cases). The results suggested that the underestimation was caused by a problem in the attenuation correction method. This was verified by the version 4.20131129 code, in which the SLV module uses an improved version of the attenuation correction method. In the results of the version 4.20131129 code, the KaPR estimates were in good agreement with the true values for moderate values of the attenuation, whereas the KaPR estimates underestimate for precipitation intensities above about 32 mm/h where $Z_{mKa} < 18$ dBZ.

The estimates, classified according to the intensity of Z_{mKa}, are useful in interpreting the characteristics of the errors. The regions where $Z_{mKa} \geq 26$ dBZ form a "horseshoe" pattern in the Pacific. Other areas that satisfy this condition occur in the mid-latitudes and in small regions of the Atlantic and Indian Oceans. Regions where Z_{mKa} is less than 18 dBZ with precipitation rates more than 4 mm/h correspond to strong precipitation events and found in the Tropics with heavy precipitation amount. In contrast, areas where Z_{mKa} is less than 18 dBZ, with precipitation rates less than 4 mm/h, are frequently observed over the subtropical waters of the Pacific Ocean, the Atlantic Ocean, and the Arabian Sea.

The performances of the DPR were slightly worse than that of the KuPR in this study, while previous works [28], [55] demonstrated better skill by the dual-frequency algorithms than by the single-frequency algorithms. One reason for this discrepancy is that the DSDs in the synthetic data were estimated from the PR 2A25 product, and that the relationship between k/Z_e and D_0 in the synthetic data was identical to that used in the algorithms. Thus, the assumptions used in the KuPR-only algorithm are consistent with the assumed DSD which provides an accuracy to the KuPR-only algorithm better than what normally can be

expected. Moreover, while the DSD estimated from the PR algorithms was regarded as a true value here, there are possible errors in the PR algorithms, which can lead to biases in the estimated DSD. In addition, differences between evaluations of the KaMS and the KaHS were small. This can be attributed to the lack of weak signals in the synthetic data. These limitations of the current synthetic data lead to a poorer performance of the DPR relative to that of the single-frequency Ku-band retrieval.

This study focused on evaluations of over-ocean estimates because the surface echo simulation at Ka-band may be problematic over the land using this method. The over-land detection routine for the KaPR is still in the developmental stage because of difficulties introduced by complex terrains. Over-land evaluations of the algorithms will be one of the future tasks. In this study, the DSD parameter μ was assumed to be 3 for the generation of the synthetic data, which is consistent with the assumption used in the current DPR-L2 algorithms. Varying the values of μ and quantifying its effect on the accuracy of the L2 algorithms, will be one of the future tasks. Current evaluations were limited to the 36 S–36 N domain observed by the TRMM satellite. Evaluations of the algorithms at higher latitudes are also planned along with a greater emphasis on snow retrievals and on modeling of snowflakes with complex and irregular shapes [56], [57].

APPENDIX A
RELATIONSHIP BETWEEN EQUIVALENT RADAR REFLECTIVITY AND NRCS AT THE SURFACE FOR THE DPR

Following previous works for a cross-track scanning geometry [33], [58], the return power P_s from the surface at an incidence angle θ with respect to nadir at a height H above the surface is related to the normalized radar cross section (NRCS) σ_L^0 of the surface by the approximation in a simple case in which the sampling is done just at the center for the antenna beam

$$P_s(\theta) = \frac{P_0 \lambda^2 G^2 L \sigma_L^0(\theta) a \cos\theta \phi_B \theta_{BP}}{512(\ln 2)\pi^2 H^2}$$

where ϕ_B and θ_B are the along- and cross-track beam widths, P_0 is the transmit power, G is the antenna gain, L is the system loss factor, λ is the radar wavelength, and a is the atmospheric attenuation along the main lobe. Also

$$\theta_{BP} = (\theta_B^{-2} + \theta_P^{-2})^{-0.5}$$

and

$$\theta_P = \frac{c\tau}{2H\theta}$$

where τ is the transmission pulsewidth and c is the speed of light.

The return power can be also expressed with equivalent radar reflectivity Z_e, and range from the antenna r (e.g., [46])

$$P_r = \frac{\pi^3 P_0 G^2 L Z_e |K_w|^2 ac\tau \phi_B \theta_B}{2^{10}(\ln 2)\lambda^2 r^2}$$

where K_w is the refractive index of water, and c is the speed of light.

At the surface (r = H), $P_s = P_r$. Therefore, an equation at Ku-band for Z_e (Z_{eKu}) and σ_L^0 (σ_{Ku}^0) and an equation at Ka-band for Z_e (Z_{eKa}) and σ_L^0 (σ_{Ka}^0) are established at the surface. A

TABLE A.I
SPECIFICATIONS OF THE DPR USED IN THE CURRENT CALCULATION

Item	Symbol	KaHS	KaMS	KuPR
Wavelength	λ	0.843 cm	0.843 cm	2.204 cm
Antenna beamwidth	θ_B	0.71°	0.71°	0.71°
Pulse width	τ	3.20 µs	1.60 µs	1.60 µs
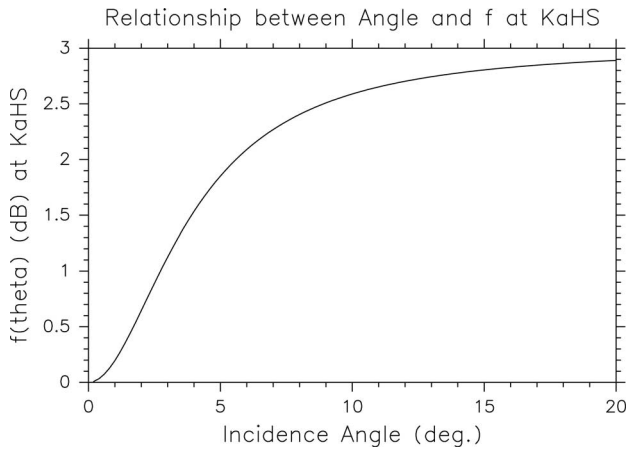
Fig. A.1. Relationship between incident angles and $f(\theta)$ in the KaHS. Unit is dB.

combination of both equations satisfies following relationship at an incidence angle θ

$$Z_{eKa} = Z_{eKu} \frac{\sigma_{Ka}^0}{\sigma_{Ku}^0} C_{KuKa} \cdot f(\theta)$$

$$C_{KuKa} = \frac{\lambda_{Ka}^4}{\lambda_{Ku}^4} \frac{|K_{wKu}|^2}{|K_{wKa}|^2} \frac{\tau_{Ku}}{\tau_{Ka}}$$

$$f(\theta) = \frac{\theta_{BPKa}}{\theta_{BPKu}} \frac{\theta_{BKu}}{\theta_{BKa}} = \frac{\sqrt{\theta_{BKu}^{-2} + \left(\frac{2}{c\tau_{Ku}} H\theta\right)^2}}{\sqrt{\theta_{BKa}^{-2} + \left(\frac{2}{c\tau_{Ka}} H\theta\right)^2}} \frac{\theta_{BKu}}{\theta_{BKa}}$$

where subscripts of Ku or Ka denote Ku-band or Ka-band. Specifications of the DPR used in the current calculation are summarized in Table A.1, and $|K_{wKu}|$, $|K_{wKa}|$, and H are assumed to be 0.9255, 0.8989, and 400 (km), respectively, here. Thus, constant "C_{KuKa}" is -16.606 (dB) at the KaMS and -19.603 (dB) at the KaHS. τ is identical between the KuPR and the KaMS, and so $f(\theta) = 1$ in the KaMS. In the KaHS, $f(\theta)$ varies with incident angles, as shown in Fig. A.1. When θ is larger, $f(\theta)$ is approaching to 3 dB, which works as an offset to differences of the constant C_{KuKa} between the KaMS and the KaHS. Thus, relationship of Z_e and σ_L^0 between the KuPR and the KaPR is obtained and it was used in the surface echo simulation at Ka-band.

ACKNOWLEDGMENT

REFERENCES

[1] A. Y. Hou *et al.*, "The global precipitation measurement (GPM) mission," *Bull. Amer. Meteor. Soc.*, to be published.

[2] M. Kojima *et al.*, "Dual-frequency precipitation radar (DPR) development on the global precipitation measurement (GPM) core observatory," in *Proc. SPIE, Earth Observ. Missions Sens. Dev. Implement. Charact. II*, 2012, vol. 8528, p. 85281A.

[3] S. Kobayashi and T. Iguchi, "Variable pulse repetition frequency for the global precipitation measurement project (GPM)," *IEEE Trans. Geosci. Remote Sens.*, vol. 41, no. 7, pp. 1741–1718, Jul. 2003.

[4] T. Miura *et al.*, "Development status of the dual-frequency precipitation radar for the global precipitation measurement," in *Proc. Int. Soc. Photogramm. Remote Sens. Tech. Comm. VIII Symp.*, Kyoto, Japan, 2010, vol. 38, Part 8, pp. 70–77.

[5] H. Masunaga and C. D. Kummerow, "Combined radar and radiometer analysis of precipitation profiles for a parametric retrieval algorithm," *J. Atmos. Ocean. Tech.*, vol. 22, pp. 909–929, Jul. 2005.

[6] S. Seto, N. Takahashi, and T. Iguchi, "Rain/no-rain classification methods for microwave radiometer observations over land using statistical information for brightness temperatures under no-rain conditions," *J. Appl. Meteorol.*, vol. 44, pp. 1243–1259, Aug. 2005.

[7] M. Grecu and W. S. Olson, "Bayesian estimation of precipitation from satellite passive microwave observations using combined radar–radiometer retrievals," *J. Appl. Meteorol. Climatol.*, vol. 45, pp. 416–433, Mar. 2006.

[8] T. Kubota *et al.*, "Global precipitation map using satelliteborne microwave radiometers by the GSMaP project: Production and validation," *IEEE Trans. Geosci. Remote Sens.*, vol. 45, no. 7, pp. 2259–2275, Jul. 2007.

[9] K. Aonashi *et al.*, "GSMaP passive microwave precipitation retrieval algorithm: Algorithm description and validation," *J. Meteorol. Soc. Jpn.*, vol. 87A, pp. 119–136, Mar. 2009.

[10] T. Kubota, S. Shige, K. Aonashi, and K. Okamoto, "Development of nonuniform beamfilling correction method in rainfall retrievals for passive microwave radiometers over ocean using TRMM observations," *J. Meteorol. Soc. Jpn.*, vol. 87A, pp. 153–164, Mar. 2009.

[11] C. D. Kummerow, S. Ringerud, J. Crook, D. Randel, and W. Berg, "An observationally generated a priori database for microwave rainfall retrievals," *J. Atmos. Ocean. Technol.*, vol. 28, pp. 113–130, Feb. 2011.

[12] S. Ramanujam, C. Radhakrishnan, D. Subramani, and B. Chakravarthy, "On the effect of non-raining parameters in retrieval of surface rain rate using TRMM PR and TMI measurements," *IEEE J. Sel. Topics Appl. Earth Observ. Remote Sens.*, vol. 5, no. 3, pp. 735–743, Jun. 2012.

[13] T. Iguchi, S. Seto, R. Meneghini, N. Yoshida, J. Awaka, and T. Kubota. (2010, Dec. 1). *GPM/DPR Level-2 Algorithm Theoretical Basis Document* [Online]. Available: http://www.eorc.jaxa.jp/GPM/doc/algorithm_e.htm

[14] T. Iguchi *et al.*, "An overview of the precipitation retrieval algorithm for the dual-frequency precipitation radar (DPR) on the global precipitation measurement (GPM) mission's core satellite," in *Proc. SPIE Earth Observ. Missions Sens.: Dev. Implement. Charact. II*, 2012, vol. 8528, p. 85281C.

[15] T. Kozu, K. Nakamura, R. Meneghini, and W. C. Boncyk, "Dual-parameter radar rainfall measurement from space: A test result from an aircraft experiment," *IEEE Trans. Geosci. Remote Sens.*, vol. 29, no. 5, pp. 690–703, Sep. 1991.

[16] R. Meneghini, T. Kozu, H. Kumagai, and W. C. Boncyk, "A study of rain estimation methods from space using dual-wavelength radar measurements at near-nadir incidence over ocean," *J. Atmos. Ocean. Technol.*, vol. 9, no. 4, pp. 364–382, Aug. 1992.

[17] R. Meneghini, H. Kumagai, J. R. Wang, T. Iguchi, and T. Kozu, "Microphysical retrievals over stratiform rain using measurements from an airborne dual-wavelength radar-radiometer," *IEEE Trans. Geosci. Remote Sens.*, vol. 35, no. 3, pp. 487–506, May 1997.

[18] R. Mardiana, T. Iguchi, and N. Takahashi, "A dual-frequency rain profiling method without the use of a surface reference technique," *IEEE Trans. Geosci. Remote Sens.*, vol. 42, no. 10, pp. 2214–2225, Oct. 2004.

[19] S. Tanelli, S. L. Durden, and E. Im, "Simultaneous measurements of Ku- and Ka-band sea surface cross sections by an airborne radar," *IEEE Geosci. Remote Sens. Lett.*, vol. 3, no. 3, pp. 359–363, Jul. 2006.

[20] R. Meneghini, L. Liao, S. Tanelli, and S. L. Durden, "Assessment of the performance of a dual-frequency surface reference technique over ocean," *IEEE Trans. Geosci. Remote Sens.*, vol. 50, no. 8, pp. 2968–2977, Aug. 2012.

[21] K. Nakamura, "Biases of rain retrieval algorithms for spaceborne radar caused by nonuniformity of rain," *J. Atmos. Ocean. Technol.*, vol. 8, pp. 363–373, Jun. 1991.

[22] T. Kozu and T. Iguchi, "Nonuniform beamfilling correction for spaceborne radar rainfall measurement: Implications from TOGA COARE radar data analysis," *J. Atmos. Ocean. Technol.*, vol. 16, no. 11, pp. 1722–1735, Nov. 1999.

[23] V. Chandrasekar *et al.*, "Potential role of dual-polarization radar in the validation of satellite precipitation measurements: Rationale and opportunities," *Bull. Amer. Meteorol. Soc.*, vol. 89, pp. 1127–1145, Aug. 2008.

[24] H. Masunaga *et al.*, "Satellite data simulation unit: Multi-sensor and multi-frequency satellite simulator package," *Bull. Amer. Meteorol. Soc.*, vol. 91, pp. 1625–1632, Dec. 2010.

[25] T. Kubota *et al.*, "Development of spaceborne radar simulator by NICT and JAXA using JMA cloud-resolving model," in *Proc. IGARSS*, 2010, pp. 1304–1307.

[26] T. Matsui *et al.*, "GPM satellite simulator over ground validation sites," *Bull. Amer. Meteorol. Soc.*, vol. 94, pp. 1653–1660, Nov. 2013.

[27] N. B. Adhikari and K. Nakamura, "Detectable rain range of spaceborne Ka-band radar estimated from TRMM precipitation radar data," *J. Atmos. Ocean. Technol.*, vol. 19, pp. 1878–1885, Nov. 2002.

[28] N. B. Adhikari and K. Nakamura, "Simulation-based analysis of rainrate estimation errors in dual-wavelength precipitation radar from space," *Radio Sci.*, vol. 38, no. 4, p. 1066, Jul. 2003.

[29] V. Chandrasekar, H. Fukatsu, and K. Mubarak, "Global mapping of attenuation at Ku- and Ka-band," *IEEE Trans. Geosci. Remote Sens.*, vol. 41, no. 10, pp. 2166–2176, Oct. 2003.

[30] J. Li and K. Nakamura, "Vertical distribution of the mirror image returns observed by TRMM PR and estimated for a 35-GHz radar," *J. Atmos. Ocean. Technol.*, vol. 22, pp. 1829–1837, Nov. 2005.

[31] S. Seto, T. Iguchi, and T. Oki, "The basic performance of a precipitation retrieval algorithm for the global precipitation measurement mission's single/dual-frequency radar measurements," *IEEE Trans. Geosci. Remote Sens.*, vol. 51, no. 12, pp. 5239–5251, Dec. 2013.

[32] T. Iguchi, T. Kozu, R. Meneghini, J. Awaka, and K. Okamoto, "Rain-profiling algorithm for the TRMM precipitation radar," *J. Appl. Meteorol.*, vol. 39, no. 12, pp. 2038–2052, Dec. 2000.

[33] R. Meneghini *et al.*, "Use of the surface reference technique for path attenuation estimates from the TRMM precipitation radar," *J. Appl. Meteorol.*, vol. 39, pp. 2053–2070, 2000.

[34] R. Meneghini, J. A. Jones, T. Iguchi, K. Okamoto, and J. Kwiatkowski, "A hybrid surface reference technique and its application to the TRMM precipitation radar," *J. Atmos. Ocean. Technol.*, vol. 21, pp. 1645–1658, Nov. 2004.

[35] T. Iguchi, T. Kozu, J. Kwiatkowski, R. Meneghini, J. Awaka, and K. Okamoto, "Uncertainties in the rain profiling algorithm for the TRMM precipitation radar," *J. Meteorol. Soc. Jpn.*, vol. 87A, pp. 1–30, Mar. 2009.

[36] J. Awaka, T. Iguchi, and K. Okamoto, "TRMM PR standard algorithm 2A23 and its performance on bright band detection," *J. Meteorol. Soc. Jpn.*, vol. 87A, pp. 31–52, Mar. 2009.

[37] M. Le and V. Chandrasekar, "Precipitation type classification method for dual frequency precipitation radar (DPR) on board the GPM," *IEEE Trans. Geosci. Remote Sens.*, vol. 51, no. 3, pp. 1784–1790, Mar. 2013.

[38] M. Le and V. Chandrasekar, "Hydrometeor profile characterization method for dual frequency precipitation radar (DPR) on board the GPM," *IEEE Trans. Geosci. Remote Sens.*, vol. 51, no. 6, pp. 3648–3658, Jun. 2013.

[39] R. Meneghini, J. A. Jones, and L. H. Gesell, "Analysis of a dual wavelength surface reference radar technique," *IEEE Trans. Geosci. Remote Sens.*, vol. GE-25, no. 4, pp. 456–471, Jul. 1987.

[40] S. Seto and T. Iguchi, "Intercomparison of attenuation correction methods for the GPM dual-frequency precipitation radar," submitted for publication.

[41] C. Kummerow, W. Barnes, T. Kozu, J. Shiue, and J. Simpson, "The tropical rainfall measuring mission (TRMM) sensor package," *J. Atmos. Ocean. Technol.*, vol. 15, no. 3, pp. 809–817, 1998.

[42] T. Kozu *et al.*, "Development of precipitation radar onboard the tropical rainfall measuring mission satellite," *IEEE Trans. Geosci. Remote Sens.*, vol. 39, no. 1, pp. 102–116, Jan. 2001.

[43] S. Shimizu, M. Yoshida, H. Hanado, and T. Higashiuwatoko, "Level 1 algorithm development of spaceborne dual-frequency precipitation radar (DPR) for GPM," in *Proc. IGARSS*, 2009, pp. I-212–I-215.

[44] J. W. Waters, "Absorption and emission of microwave radiation by atmospheric gases," in *Methods of Experimental Physics*, vol. 12, Part B, *Radio Astronomy*, M. L. Meeks, Ed. New York, NY, USA: Academic Press, 1976, pp. 142–176.

[45] F. T. Ulaby, R. K. Moore, and A. K. Fung, *Microwave Remote Sensing: Active and Passive*, vol. I. Norwood, MA, USA: Artech House, 1981, p. 456.

[46] R. Meneghini and T. Kozu, *Spaceborne Weather Radar*. Norwood, MA, USA: Artech House, 1990.

[47] P. W. Rosenkranz, "Shape of the 5 mm oxygen band in the atmosphere," *IEEE Trans. Antennas. Propag.*, vol. 23, no. 4, pp. 498–506, Jul. 1975.

[48] T. Kubota, M. Satoh, T. Nasuno, S. Seto, T. Iguchi, and R. Oki, "Development of cloud liquid water database using global cloud-system resolving model for GPM/DPR algorithm," in *Proc. IGARSS*, 2012, pp. 350–353.

[49] F. T. Ulaby, R. K. Moore, and A. K. Fung, "Relating the microwave backscattering coefficient to leaf area index," *Remote Sens. Environ.*, vol. 14, pp. 113–133, 1984.

[50] L. Prevot, I. Champion, and G. Guyot, "Estimating surface soil moisture and leaf area index of a wheat canopy using a dual-frequency (C and X bands) scatterometer," *Remote Sens. Environ.*, vol. 46, pp. 331–339, 1993.

[51] M. S. Moran, A. Vidal, D. Troufleau, Y. Inoue, and T. A. Mitchell, "Ku- and C-band SAR for discriminating agricultural crop and soil conditions," *IEEE Trans. Geosci. Remote Sens.*, vol. 36, no. 1, pp. 265–272, Jan. 1998.

[52] S. Seto and T. Iguchi, "Rainfall-induced changes in actual surface backscattering cross sections and effects on rain-rate estimates by spaceborne precipitation radar," *J. Atmos. Ocean. Technol.*, vol. 24, no. 10, pp. 1693–1709, Oct. 2007.

[53] R. Gunn and G. G. Kinzer, "The terminal velocity of fall for water droplets in stagnant air," *J. Atmos. Sci.*, vol. 6, no. 4, pp. 243–248, Aug. 1949.

[54] D. A. Short, K. Nakagawa, and T. Iguchi, "Empirical test of theoretically based correction for path integrated attenuation in simulated spaceborne precipitation radar observations," *IEEE J. Sel. Topics Appl. Earth Observ. Remote Sens.*, vol. 5, no. 3, pp. 900–935, Jun. 2012.

[55] N. B. Adhikari and T. Iguchi, "Effect of raindrop size distribution variability in dual-frequency radar rain retrieval algorithms assessed from disdrometer measurements," *IEEE Geosci. Remote Sens. Lett.*, vol. 3, no. 2, pp. 197–201, Apr. 2006.

[56] G. Liu, "A database of microwave single-scattering properties for nonspherical ice particles," *Bull. Amer. Meteorol. Soc.*, vol. 89, pp. 1563–1570, Oct. 2008.

[57] L. Liao, R. Meneghini, H. K. Nowell, and G. Liu, "Scattering computations of snow aggregates from simple geometrical particle models," *IEEE J. Sel. Topics Appl. Earth Observ. Remote Sens.*, vol. 6, no. 3, pp. 1409–1417, Jun. 2013.

[58] T. Kozu, "A generalized surface echo radar equation for downlooking pencil beam radar," *IEICE Trans. Commun.*, vol. E78-B, pp. 1245–1248, 1995.

Takuji Kubota (M'07) received the B.S., M.S., and Ph.D. degrees in science from Kyoto University, Kyoto, Japan, in 1999, 2001, and 2004, respectively.

From 2004 to 2005, he was a Postdoctoral Researcher with Disaster Prevention Research Institute, Kyoto University, and with Japanese Science Technology Agency from 2005 to 2007. Since 2007, he has been a Researcher with Earth Observation Research Center, Japan Aerospace Exploration Agency, Tsukuba, Japan. His current research interests include algorithm development for spaceborne microwave radar and radiometers for the TRMM, GPM, and EarthCARE missions.

Dr. Kubota is a member of the Remote Sensing Society of Japan, Meteorological Society of Japan, Japan Geoscience Union, American Meteorological Society, and American Geophysical Union.

Naofumi Yoshida received the B.S. and M.S. degrees from the Tohoku University, Sendai, Japan, in 1998 and 2000 respectively.

Since 2003, he has been with the Remote Sensing Technology Center of Japan, Tokyo. His current interests include low-level algorithm development and calibration for spaceborne microwave radar for the TRMM and GPM missions.

Shinji Urita received the B.S. and M.S. degrees in geography from the Tokyo Metropolitan University, Hachioji, Japan, in 2010 and 2012 respectively.

Since 2012, he has been with the Remote Sensing Technology Center of Japan, Tokyo. He is current in charge of integration, test, and validation in the Global Precipitation Measurement /Dual-Frequency Precipitation Radar level 2 and 3 algorithms.

Mr. Urita is a member of Meteorological Society of Japan and Japan Society of Hydrology and Water Resources.

Toshio Iguchi (M'97) received the B.Sc. degree from Hokkaido University, Sapporo, Japan, in 1976, the M.Sc. degree from the University of Tokyo, Tokyo, Japan, in 1978, and the Ph.D. degree from York University, Toronto, ON, Canada, in 1983.

Since 1985, he has been with the National Institute of Information and Communications Technology (formerly the Communications Research Laboratory), Japan. From 1991 to 1994, he visited the NASA/Goddard Space Flight Center, MD, performing the U.S.–Japan collaborative experiment for measuring rain using airborne radar. Since then, he has focused primarily on issues related to the remote sensing of precipitation from space.

Shinta Seto (M'10) received the B.E., M.E., and Ph.D. degrees from the University of Tokyo, Tokyo, Japan, in 1998, 2000, and 2003, respectively.

From 2003 to 2006, he was a Postdoctoral Researcher with the National Institute of Information and Communications Technology (formerly the Communications Research Laboratory), Japan, where he worked on the development of spaceborne dual-frequency precipitation radar. From 2006 to 2012, he was with the Institute of Industrial Science, the University of Tokyo, Japan. Since 2012, he has been with Nagasaki University, Nagasaki, Japan. His current research interests include precipitation retrieval using microwave remote sensing and its application to water cycle studies.

Robert Meneghini (M'80–SM'96) received the bachelor degrees in philosophy and electrical engineering from the University of Illinois, Champaign, IL, USA, the M.S. degree in electrical engineering from University of Michigan, Ann Arbor, MI, USA, and the Ph.D. degree in electrical engineering from Kyoto University, Kyoto, Japan.

Since 1974, he has been with the NASA/Goddard Space Flight Center, Greenbelt, MD, USA and has worked on a variety of problems related to the radar/radiometer remote sensing of rain and cloud.

Dr. Meneghini is a member of the NASA Precipitation Measurement Missions Science team and a member of American Geophysical Union.

Jun Awaka (M'84) received the B.E. and Dr .Eng. degrees from Hokkaido University, Sapporo, Japan, in 1973 and 1984, respectively.

From 1975 to 1991, he was with the Communication Research Laboratory, Tokyo, Japan. From 1991 to 2008, he was with Hokkaido Tokai University, Sapporo, Japan, and since 2008, he has been a Professor with Sapporo Campus, Tokai University, Sapporo, Japan. His current interest includes rain-type classification in rain observation from space.

Hiroshi Hanado (M'00) received the B.S. and M.S. degrees in geophysics from Kyoto University, Kyoto, Japan, in 1987 and 1989, respectively. He joined the Communications Research Laboratory (CRL) (currently called the National Institute of Information and Communications Technology), Tokyo, Japan, in 1989, where he has been engaged in the study of microwave remote sensing, particularly on rain radar.

He is currently a member of the Global Precipitation Measurement/Dual-Frequency Precipitation Radar Project Team, Space Applications Mission Directorate, Japan Aerospace Exploration Agency, Tokyo.

Satoshi Kida received the B.E., M.E. and Ph.D. degrees in aerospace engineering from Osaka Prefecture University, Sakai, Japan, in 2005, 2007, and 2010, respectively.

He works with Earth Observation Research Center, Japan Aerospace Exploration Agency, Tsukuba, Japan. His research interests include algorithm development for spaceborne microwave radar and radiometers and validation of rainfall retrievals.

Riko Oki received the Dr. Sci. degree in geophysics from the University of Tokyo, Tokyo, Japan, in 1995.

She joined the Remote Sensing Technology Center of Japan, Tokyo, in 1995. Since 1998, she has been with the National Space Development Agency of Japan (currently called the Japan Aerospace Exploration Agency), Tokyo. She has been engaged in research on meteorology and climatology. She is currently a Chief Scientist with the Tropical Rainfall Measuring Mission/Global Precipitation Measurement Project Group, Earth Observation Research Center, Japan Aerospace Exploration Agency.